Current Topics in
Electrochemistry
Vol. 25, 2023

Original Article

Evaluation of the performance of N-doped graphene, synthesized by solvothermal method, as anode for Na-ion and Li-ion batteries

Ali İhsan Kömür and Edip Bayram*

Akdeniz University, Department of Chemistry, Institute of Natural and Applied Sciences,
Dumlupınar Boulevard, Antalya, Türkiye.

ABSTRACT

Graphene is a promising electrode material that is used as anode in commercial Li-ion and Na-ion batteries due to its extraordinary properties such as high electrical conductivity and chemical resistance. Moreover, doping graphene with heteroatoms can modulate the surface electronic charge density, leading to high capacity and stability in ion batteries. On the other hand, the capacity and performance of graphene are governed by the type of doped atom and pore structure depending on the production method. In this study, N-doped graphene (N-GN) was produced by a solvothermal route and characterized. The electrochemical behaviors of N-GN were determined through the cyclic voltammetry (CV), galvanostatic charge/discharge (GCD) and Dunn & Trassati methods. N-GN exhibited a superior long-term performance of 347 mAh.g^{-1} after 250 cycles at 0.5 A.g^{-1} for Li$^+$ and 136 mAh.g^{-1} for Na$^+$, maintaining 92% of the initial capacity with a Coulombic efficiency of >98%. Long-term durability and performance characteristics were attributed to the stability of the solid electrolyte interface (SEI) based on the evaluation of electrochemical impedance spectra taken every 50 cycles during 250 charge/discharge cycles.

KEYWORDS: nitrogen-doped graphene, sodium-ion battery, lithium-ion battery, anode, energy storage.

1. INTRODUCTION

Issues such as rising fuel costs due to diminishing fossil fuel reserves, environmental pollution and global warming have increased the need for the development of sustainable and highly efficient electrochemical energy storage (EES) systems [1-4]. Although lithium-ion batteries (LIBs) fulfil the requirements for energy storage, the limited resources of Li make it necessary to increase the lifetime and the capacity of LIBs as well as their recycling. The energy density, the cyclic performance, and the rate capability of the LIBs are greatly dependent on the chemical and physical properties of the electrode materials [5]. Therefore, research on LIBs in recent years has been focused on the development of high-performance anode materials. In this context, various alloying (e.g., Si, Sn) [6, 7], conversion (MOx, M: transition metal) [8] and insertion (e.g., graphite, MXene) -type [9] anode materials have been developed based on the Li$^+$ storage reaction. However, low coulombic efficiency, unstable solid electrolyte interface (SEI) formation, large potential hysteresis and poor cycle life caused by high volumetric variations during charging/ discharging of alloying and conversion-type materials have led the studies to be directed towards carbon materials [10]. Carbon materials also have the advantages of cost effectiveness and abundant availability. Graphite is commonly used as an anode in commercial LIBs because it is cheap, non-toxic and has a charge/discharge

---

*Corresponding author: ebayram@akdeniz.edu.tr

plateau below 0.2 V. However, low theoretical specific capacity (372 mAh.g^{-1}) has necessitated the development of high-capacity carbon-based anodes instead of graphite. Graphene has been extensively studied as a high-performance anode candidate in LIBs due to its high conductivity, chemical resistance, and high specific surface area. However, the LIB anode performance of graphene did not meet expectations due to agglomeration of graphene nanosheets because of electrochemical processes during charge/ discharge, formation of thick SEI due to high surface area and low first-cycle coulombic efficiency [11, 12]. On the other hand, incorporation of heteroatoms (e.g., N, Si, S, etc.) into graphene structure has been shown to facilitate charge transfer and electrode-electrolyte interactions in graphene, thus significantly increasing its electrical conductivity and surface hydrophilicity [13, 14]. In addition, depending on the production process, parameters such as the amount of dopant and the pore structure can be adjusted [15].

Sodium-ion batteries (SIBs) have attracted considerable attention as an alternative energy storage device in recent years due to their acceptable energy density (80-130 Wh.kg^{-1}), affordability and availability of materials. Moreover, owing to the similar chemical properties of Na^+ to Li^+, such as its monovalence, acceleration is expected in the development of SIBs [16-18]. These features make SIBs a promising technology for high-volume energy storage such as grid applications. Although the anodes used in LIBs were also tested for SIBs, slow reaction kinetics and low stability were generally observed in these anodes due to the different Levis acidity character and ~34% larger radius of Na^+ than Li^+ [19, 20]. Therefore, the anode material to be used in LIBs and SIBs must have a suitable crystal and pore structure as well as a proper chemical structure to store these ions. In this context, a detailed analysis of the behavior of Na^+ and Li^+ ions towards a well-defined common anode may provide deep insights that can lead to designing SIB and LIB anodes with high capacity and performance.

In this study, high surface area nitrogen-doped graphene (N-GN) was fabricated by a rational and scalable solvothermal procedure. The fabricated N-GN nanostructures were physiochemically characterized and then evaluated by electrochemical characterization techniques in terms of their potential applications as anode materials in half cells. This study provides valuable insights into the performance of nitrogen-doped graphene-based anodes for SIBs and LIBs in terms of interfacial interactions. It has been shown that it is possible to tune the interlayer spacing of graphene layers, thereby enhancing Na^+ and Li^+ storage capacity with superior performance such as rate capability and cyclic stability.

2. MATERIALS AND METHODS

2.1. Chemicals and materials

Chemicals with a high degree of purity that do not require further purification were used in all the experiments. Na (Sodium), N,N-Dimethylformamide (DMF) and HCl used for the synthesis of N-GN were purchased from Merck. N-Methyl-2-pyrrolidone (NMP), Ethylene Carbonate (EC), Dimethyl Carbonate (DMC), Fluoroethylene-carbonate (FEC), $NaPF_6$, $LiPF_6$, Li sheet and Carbon Black which were used in the preparation of half cells were purchased from Sigma-Aldrich. Binder PVdF (Polyvinylidendifluoride) and seperator glass filter were from Alpha-Aesar while Polyethylene (PE) was obtained from SOLUPOR®. Ultrapure water (18.2 MΩ) from Milli-Q UV water purification system was used if necessary.

2.2. Solvothermal synthesis of the N-GN

The details of the steps followed in the synthesis of nitrogen-doped graphene by solvothermal method are given in our previous study [21]. Briefly, adequate amounts of sodium as a reducing agent and DMF as an N and C source were put into the Teflon chamber of a solvothermal reactor (Bergof, Germany) under argon atmosphere. After heating the mixture at 190 °C for 72 h, a solid yellow intermediate was obtained. Unlike our previous study [21], after obtaining the liquid mixture of the intermediate with pure water, the pH of the mixture was adjusted to 13 with NaOH and dried at 170 °C. The product was then subjected to pyrolysis in a horizontal furnace at 750 °C under Ar atmosphere and the final product was labeled as N-GN.

2.3. Physicochemical characterization

The specific surface area and pore size distributions were calculated using the Brunauer-Emmett-Teller (BET) method via N_2 adsorption-desorption isotherm data acquired by Micromeritics ASAP 2010 at 77°K. A scanning electron microscope (SEM) FEI QUANTA FEG 250 with an operating voltage of 10 kV was used to analyse the surface morphology of the samples. An X-ray diffractometer (BRUKER D8 ADVANCED TWIN-TWIN) operating at 40 kV/ 30 mA with a Cu Kα (λ= 1.54056 Å) radiation source was used to record the X-ray diffraction (XRD) patterns of the powder samples. The elemental composition of the surface was determined using an X-ray photoelectron spectrometer (XPS) (Thermo Fisher) at the characteristic energy of 1486.6 eV (Al Kα). The ordered and disordered structures of the samples were determined by a Renishaw inVia Raman microscope equipped with a 532 nm laser excitation source.

2.4. Electrochemical methods and assembly of half cells

The electrochemical properties of N-GN, synthesized as anode materials for SIBs and LIBs, were assessed in CR-2032 coin-type half-cells. Na-Li metal disks were utilized for both counter and reference, and the N-GN-based electrodes were employed as working electrodes. The electrode was prepared by mixing N-GN, carbon black and binder (PVdF) in NMP in a weight ratio of 80:10:10. The prepared slurry was coated onto the copper foil collector at a mass loading of ~1.0 mg.cm^{-2} and dried overnight in a vacuum oven at 80 °C. Electrolyte-wetted glass fibre or PE was used as the separator. The electrolyte solutions were prepared by dissolving 1.0 M $NaPF_6$ or $LiPF_6$ in a mixture of EC/DMC (1:1 by volume) containing 5 wt% FEC. The half-cells were assembled in a high-purity argon-filled glove box (MBraun, Germany).

The electrochemical characterization of the assembled half cells was carried out at room temperature by a potentiostat/galvanostat (IVIUM-Vertex). Galvanostatic charge/discharge (GCD) curves were obtained in the potential range of 0.010-3.0 V (vs. Na/Na^+ and Li/Li^+) at constant current density. Cyclic voltammetry (CV) voltammograms were obtained in the operating potential range 0.010 V-3.0 V (vs. Na/Na^+ and Li/Li^+). Electrochemical impedance spectroscopy (EIS) studies were carried out at 0.50 V and frequency range of 250 kHz-0.001 Hz with an amplitude of 10 mV.

3. RESULTS AND DISCUSSION

3.1. Physicochemical characterization of N-GN sample

The production of N-GN was carried out by an easily scalable bottom-up synthesis strategy based on the solvothermal method. The synthesis of N-doped graphene starts with the formation of dimethylamine and highly reactive carbonyls by decarbonylation of DMF above 153 °C. Under solvothermal conditions and in the presence of metallic sodium catalyst, these species react rapidly to form C macrostructures [22]. Pyrolysis of these macrostructures in an Ar atmosphere at temperatures above 600 °C leads to self-assembly of graphene architectures.

SEM images taken at various magnifications in dry powder form (Figure 1 a,b) show that N-GN comprises a macro structure above the micron size consisting of multilayer graphene plates displaying a wrinkled silk wave-like appearance, which is specific to graphene. Moreover, the presence of meso-micro pores as well as macropores with a size of about 300 nm is clearly visible. The nitrogen adsorption/desorption isotherm of N-GN (inset of Figure 2a) is consistent with Type-IV isotherms with H4-type hysteresis loop revealing the mesoporous structure [17]. The S_{BET} value calculated by Brunauer-Emmett-Teller (BET) method was 1289 m^2.g^{-1}. The average pore diameter was calculated as 3.46 nm by the Barrett-Joyner-Halenda (BJH) method and a sharp peak at 3.7 nm was observed in the pore size distribution plot (Figure 2a). Moreover, the meso- and micropore volumes were calculated as 0.6534 cm^3.g^{-1} and 0.0011 cm^3.g^{-1}, respectively. These findings further confirm the mesoporous structure of N-GN. In this context, the mesoporous structure of N-GN indicates that it can facilitate ion and mass transfer in LIBs and SIBs, while also having a high specific capacity due to its large surface area.

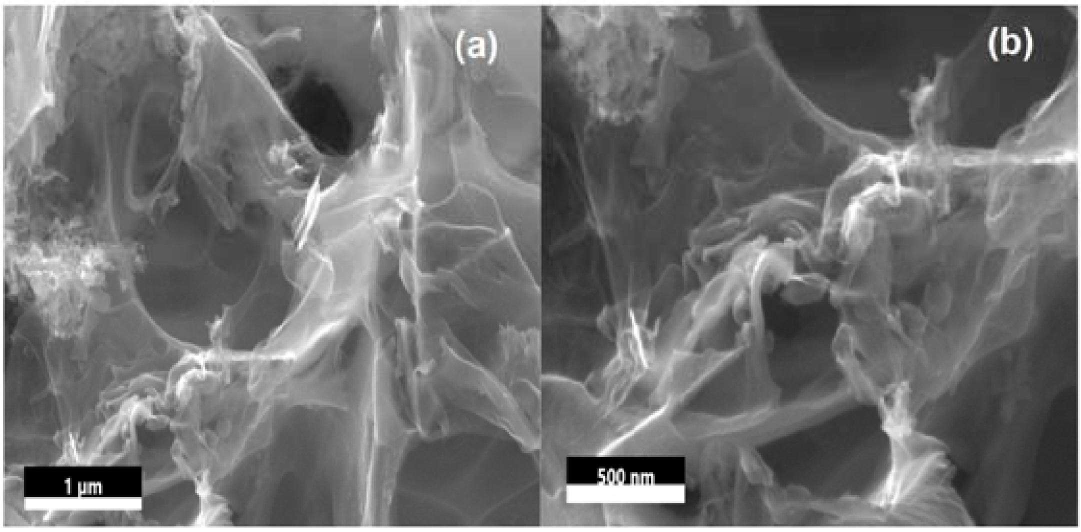

Figure 1. SEM images of N-GN taken at different magnifications.

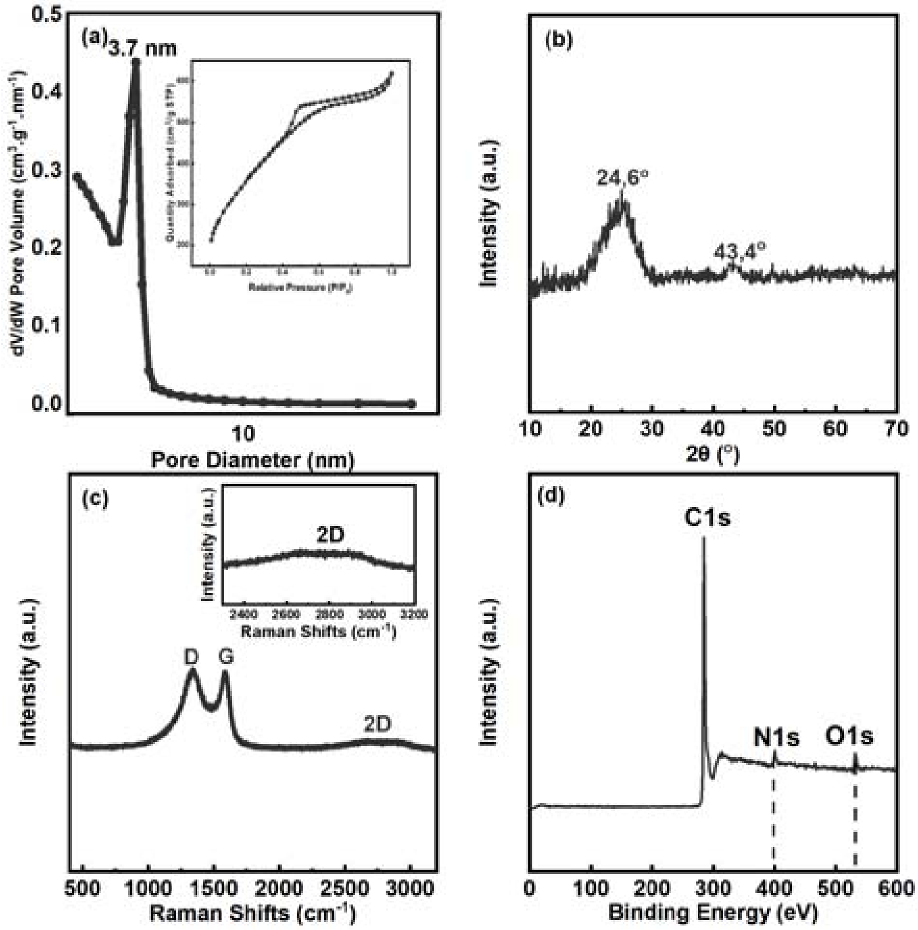

Figure 2. BJH pore size distribution and BET adsorption and desorption isotherms (in-set) (a), XRD patterns (b), Raman spectra (in-set is the enlargement of the 2D region) (c), and XPS survey spectra (d) for N-GN.

The crystalline structures were assessed through the XRD analysis. The XRD pattern of the N-GN (Figure 2b) displayed two broad distinct diffraction peaks at around 2θ=24.6° and 2θ=43.4° corresponding to the graphitic-like [002] planes and unexfoliated graphene [101], respectively [23]. The full-width at half-maximum (FWHM) value of 5.463, along with the obvious enlargement in [002] peak, revealed the formation of irregularly separated graphene sheets for N-GN with respect to the graphite. The interlayer spacing (d, nm), calculated from the Bragg equation was 0.36 nm, which was larger than that of graphite (d=0.334 nm) [24]. It's known that graphite's narrow layer to layer d-spacing limit its application as an anode material, especially in SIBs. Therefore, it was expected that the samples having larger interlayer d-spacing could be beneficial for intercalation of Na^+ and Li^+ ions. Raman spectroscopy provides valuable information on the number of graphene layers, the quality of the structure and the presence of defects/ impurities. Three important characteristic bands were observed at 1339 cm^{-1} indicating the presence of defect (D), 1580 cm^{-1} for graphenic conjugation (G) and around 2670 cm^{-1} which is indicative of the number of layers and defects in the graphene structure and the presence of N (Figure 2c). Moreover, the intensity ratio of the D and G bands (I_D/I_G), which depends on the presence of defects in the graphene sheets, was calculated as 1.34, indicating the presence of abundant defects in the N-GN structure. The surface chemical properties and elemental composition of N-GN sample was analyzed by XPS. The full-range XPS spectra revealed three main peaks located at about 284.1 eV, 399.5 eV and 531.1 eV attributed to C1s, N1s and O1s, respectively, thus confirming the success of N doping along with the purity of the samples (Figure 2d). The relative surface element concentrations calculated by Gaussian peak fitting based on the Shirley baseline were 93.2%, 3.60%, and 2.86% for C, N, and O, respectively. The high carbon, moderate N and relatively low oxygen atom ratio of N-GN indicates the high quality of the product.

3.2. Electrochemical characterization of N-GN sample

The electrochemical properties of the N-GN sample were investigated in the corresponding half cells by means of CV, Dunn & Trasatti, GCD and EIS. The CV voltammograms obtained for the first three cycles at room temperature between 0.01-3.00 V and at a potential scan rate of 0.5 $mV.s^{-1}$ for Na^+ and Li^+ containing half cells are given in Figure 3a and b, respectively.

Apparently, the sharp irreversible peak observed at 0.19 V (vs. Na/Na^+) in the first cycle of Na^+ is attributed to the formation of stable SEI, which disappears in subsequent cycles (Figure 3a). In cycles 2nd and 3rd, a broad shoulder in the cathodic direction, quite stable in the range 0.9-1.5 V, and a peak at 0.51 V were observed. The anodic broad peak centered at ~0.29 V is assigned to the desodiation of Na^+ ions from the interlayers of N-GN. Similarly, for Li^+, a peak at 0.52 V (vs. Li/Li^+) attributed to stable SEI formation was observed in the first cycle and disappeared in the subsequent cycles, exhibiting overlapping voltammograms (Figure 3b). Here, it can be concluded that the lithiation process occurs mainly below 0.32 V, and the delithiation process occurs at 0.25 V with a shoulder at 1.1 V. GCD profiles obtained from 1-10 cycles, collected at a current density of 0.1 $A.g^{-1}$ and potential range of 0.01-3.00 V, are plotted in Figure 3c and d. N-GN exhibited a wide voltage plateau below 0.70 V (vs. Na/Na^+) and 0.43 V (vs. Li/Li^+) in the first cycle, with high sodiation and lithiation capacities of 754 and 1302 $mAh.g^{-1}$ and delivered reversible capacities of 184 and 515 $mAh.g^{-1}$ at 10th cycle, respectively. In the sodiation profile for 10th cycle, two regions, capacitive (1.5-0.15 V vs. Na/Na^+) and diffusive (below 0.15 V vs. Na/Na^+), were observed, while in the lithiation profile (1.5-0.60 V and 0.60-0.13 V vs. Li/Li^+) an additional plateau was observed below 0.13 V indicating diffusion of Li^+ into the internal pores of N-GN [25]. The quantitative contribution of capacitive and diffusive currents to the energy storage mechanism can be analyzed through the CV data performed at different scan rates according to the Dunn & Trasatti method [15].

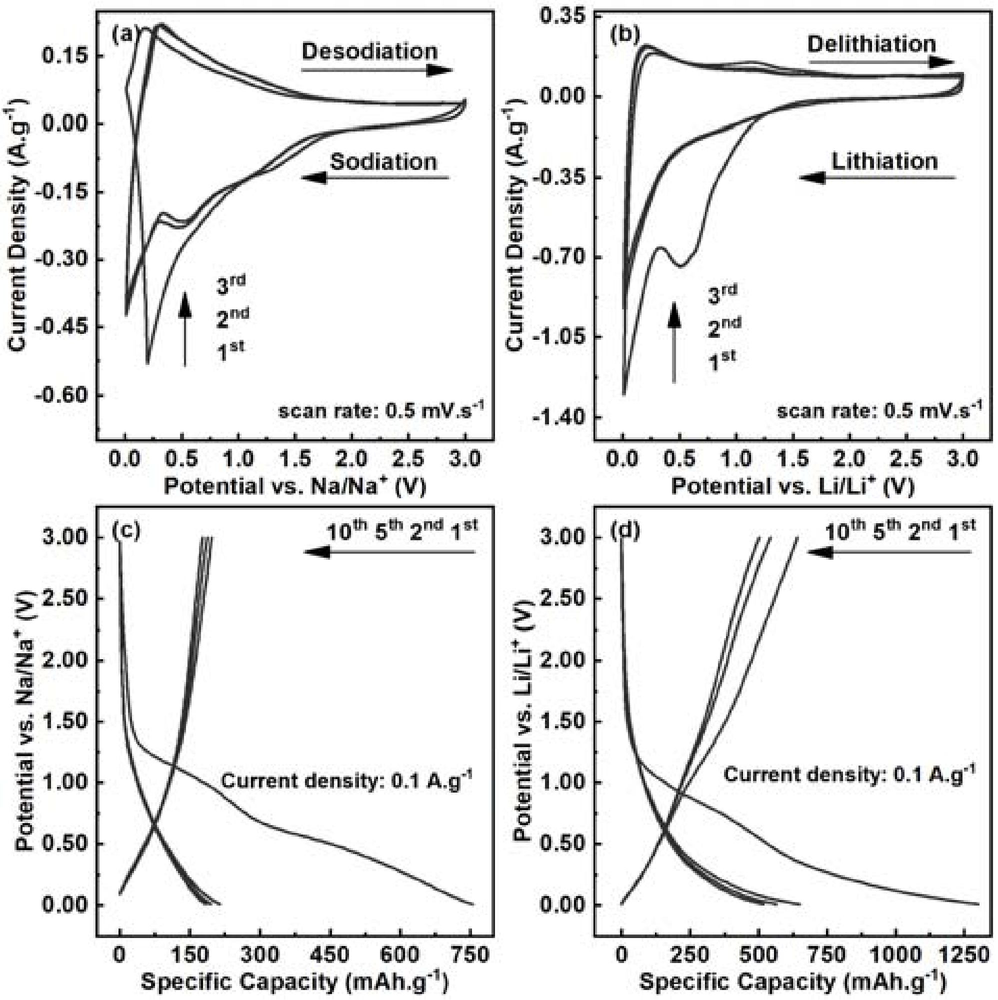

Figure 3. CVs of N-GN/Na^+ (a) and N-GN/Li^+ (b) half-cells performed at the potential range of 0.01-3.00 V and a potential scan rate of 0.5 $mV.s^{-1}$. The GCD profiles of N-GN/Na^+ (c), and N-GN/Li^+ (d) collected at a current density of 0.1 $A.g^{-1}$ and 0.01-3.00 V potential range.

The CVs obtained at various scan rates for Na and Li half-cells are given in Figure 4a and c, respectively. Here, the fact that the peak positions in both the cathodic and anodic directions do not change with increasing scan rate proves the reversibility of the electrochemical reactions responsible for the charge/discharge processes. Interestingly, diffusion-controlled currents play a significant role in the sodiation process at potentials below 1.73 V, while diffusion-controlled desodiation primarily occurs at 0.18 V (Figure 4b). On the other hand, diffusion-controlled lithiation occurred below 0.80 V and delithiation mainly above 0.90 V (Figure 4d). According to Trasatti data corresponding to the contributions at a scan rate of 0.0 $mV.s^{-1}$, the capacitive contribution for Na^+ was calculated as 63% while for Li^+ it was 47% (inset of Figure 4b and d). Moreover, when the scan rate was increased from 0.2 $mV.s^{-1}$ to 1.0 $mV.s^{-1}$, a 17% decrease in diffusion-controlled currents was observed for Li^+, whereas for Na^+ it was only 14%. When the findings are considered concurrently, it becomes apparent that Na^+ intercalates into the mezo- and macro-pores of N-GN, while Li^+ additionally intercalate into the regular crystal vacancies in the inner micro-pores. The rate performance tests were carried out to evaluate the effect of pore structure on mass transfer and to reveal the advantages of N-GN as an anode for SIBs and LIBs. Figure 5a shows that

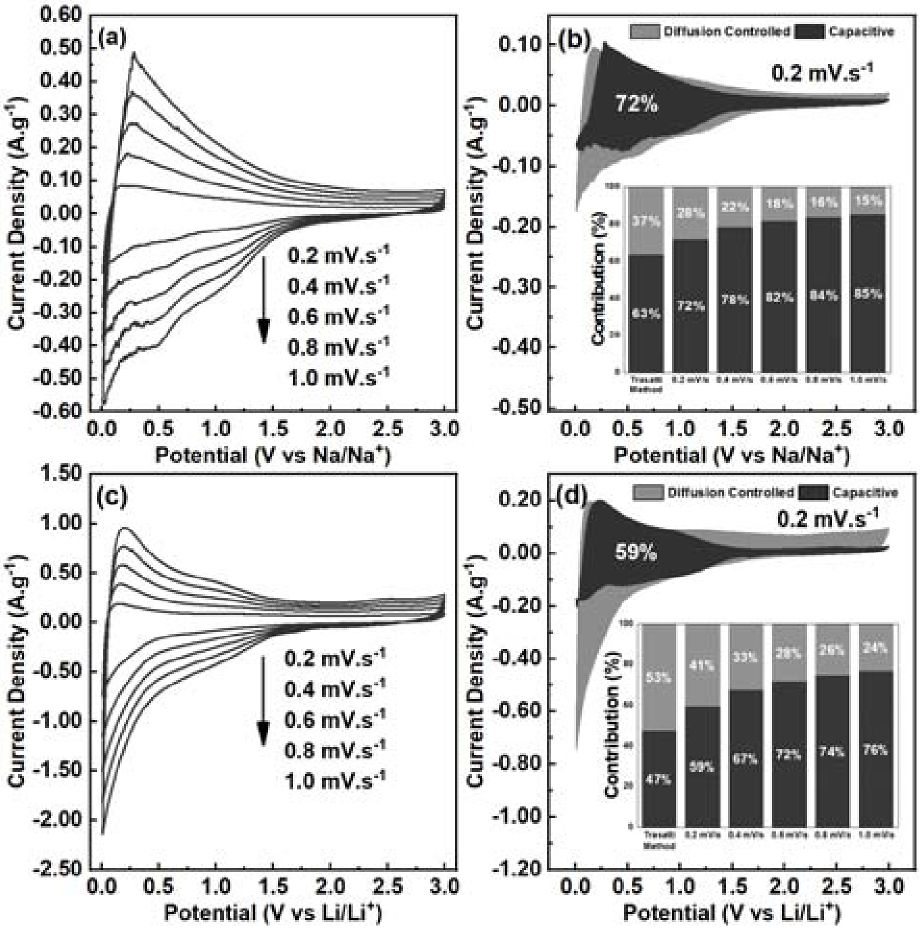

Figure 4. The CVs at various scan rates for N-GN/Na$^+$ (a) and N-GN/Li$^+$ (c). The contribution ratio of the capacitive and diffusion-controlled processes at 0.2 mV.s^{-1} for N-GN/Na$^+$ (b) and N-GN/Li$^+$ (d). The in-sets of (b), and (d) show the ratio of capacitive and diffusion-controlled processes at various scan rates and extrapolation by Trasatti Method.

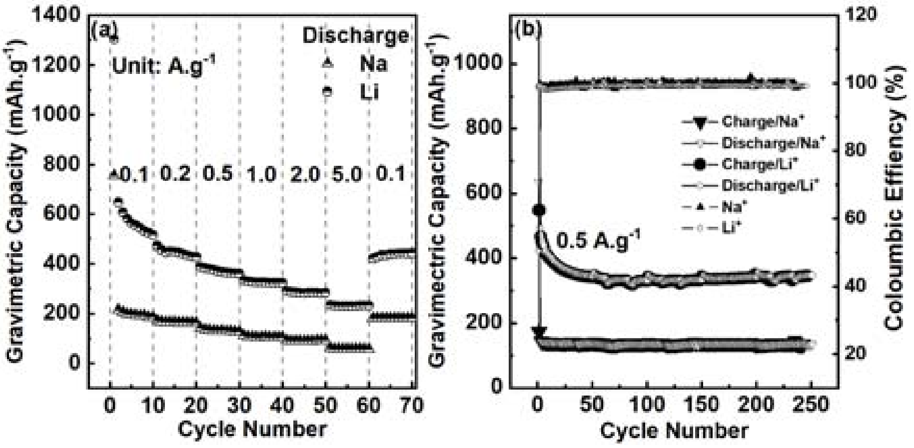

Figure 5. Rate capability behavior of N-GN at current densities between 0.1-5.0 A.g^{-1} (a), and the cyclic performance of the half cells at a current density of 0.5 A.g^{-1} (b).

N-GN provides specific capacities at the end of each ten cycle of 184, 161, 126, 102, 90, 56, and 179 mAh.g^{-1} for Na$^+$ and 515, 426, 360, 321, 282, 231 and 441 mAh.g^{-1} for Li$^+$ at current densities of 0.1, 0.2, 0.5, 1.0, 2.0, 5.0 and 0.1 A.g^{-1}, respectively. It is clearly seen that the rate of decrease in capacity with increasing current density is much lower for Na$^+$ than for Li$^+$ and N-GN exhibits high performance for both ions even at very high current density of 5.0 A.g^{-1}. It was also observed that after the 60th cycle, when a current density of 0.1 A.g^{-1} was reapplied, the initial capacities were restored. These results demonstrate the formation of stable SEI on the surface of N-GN for both ions and further confirm the above discussion on the ion storage mechanism in the N-GN anode.

At this point, the long-term charge-discharge performance at 0.5 A.g^{-1}, which has a relatively high current density, can provide significant information in terms of their real-life applicability. During the prolonged performance evaluation of N-GN for Li$^+$ (Figure 5b) the capacity decreased from 491 mAh.g^{-1} to 332 mAh.g^{-1} upto the first 70 cycles. However, after the 70th cycle, the capacity increased most probably due to the formation of new ion channels and reached 347 mAh.g^{-1} at the end of 250 cycles. Moreover, the Na$^+$ half-cell demonstrated outstanding performance by maintaining 92% of its initial capacity of 136 mAh.g^{-1} at the end of 250 cycles. It is to be noted that, both Na$^+$ and Li$^+$ half-cells exhibited Coulombic efficiencies of >98% over 250 cycles (Figure 5b). EIS of the Na$^+$ and Li$^+$ half-cells was performed at 0.50 V and 250 kHz-0.001 Hz for the first and each 50 subsequent GCD cycles at a current density of 0.5 A.g^{-1}. Nyquits plots obtained from Na$^+$ and Li$^+$ half-cells are given in Figure 6a and b, respectively, together with well-fitted lines

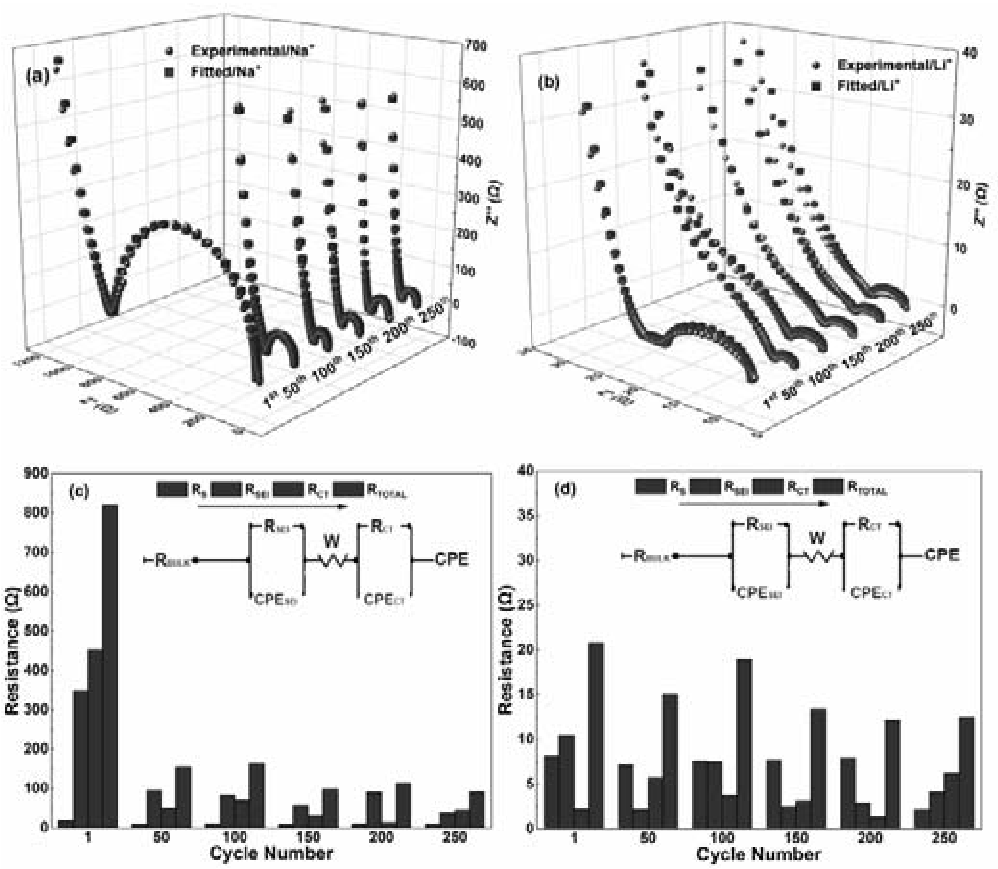

Figure 6. Nyquist plots (a, b) and corresponding resistance elements calculated from equivalent circuits (c, d) of Na$^+$ (a, c) and Li$^+$ (b, d) half-cells.

through resistive elements in their equivalent circuits.

For Na^+ half-cell, after a huge impedance due to SEI formation in the first cycle, all impedance data taken after the 50th cycle show a semicircle in the high frequency region followed by a short Walburg region and then a steep line in the low frequency region indicating ideal capacitive behavior (Figure 6a). In the of case Li^+ half-cell, in addition to the semi-circle, a relatively long Walburg line in the mid-frequency region and a low-angle capacitance line in the low-frequency region were observed. For both half-cells, the relatively short Walburg region in the mid-frequency region indicates an excellent ion diffusion efficiency [26] (Figure 6b). Figure 6c and d present the variations of the resistance elements over 250 cycles for Na^+ and Li^+ half-cells. In the Na^+ half-cell, very high interfacial resistance (R_{SEI}) and correspondingly high charge transfer resistance (R_{ct}) were observed in the first cycle, indicating the formation of a thick SEI. The blockage of micropores by the formation of a thick SEI may be the reason for the relatively low Na^+ capacity. After the first cycle, although the amount of the resistive elements varied, the total resistance (R_{TOTAL}) remained almost constant around 164 Ω up to the 100th cycle and then decreased in accordance with the high stability observed in Figure 5b and was calculated to be 91 Ω at the 250th cycle. In the Li^+ half-cell, in contrast to Na^+, the R_{TOTAL} of 20 Ω in the first cycle, which is quite low for Li-ion batteries, decreased further to 12 Ω in the 250th cycle due to the formation of a thin and stable SEI which explains the high capacity and exceptional long-term performance (Figure 5d).

4. CONCLUSIONS

Mesoporous high surface area nitrogen-doped graphene (N-GN) was synthesized *via* a scalable bottom-up solvothermal process. N-GN exhibited a superior long-term performance of 347 $mA.g^{-1}$ after 250 cycles at 0.5 $A.g^{-1}$ for Li^+ and its performance was attributed to the formation of relatively thin SEI and diffusion of Li^+ into the inner pores of N-GN. The superior rate capability and capacity retention capability observed in the Na^+ half-cell was linked to the storage of Na^+ in mesopores of N-GN with high capacitive currents ratio. The results should be supported by further studies by techniques such as *in-situ* operando XRD or Raman.

ACKNOWLEDGEMENTS

We are grateful to the support given by Akdeniz University Scientific Research Projects Coordination Unit for this study under the project number of FDK-2021-5697. The authors would also like to thank Yüksel Tohum Corp.

CONFLICT OF INTEREST STATEMENT

The authors declare no conflict of interest.

REFERENCES

1. Zhang, C., Lv, W., Tao, Y. and Yang, Q.-H. 2015, Energy Environ. Sci., 8, 1390-1403.
2. Titirici, M. -M., White, R. J., Brun, N., Budarin, V. L., Su, D. S., del Monte, F., Clark, J. H. and MacLachlan, M. J. 2015. Chem. Soc. Rev., 44, 250-290.
3. Bayram, E., Kızıl, Ç. and Ayrancı, E. 2018, Water Sci. Technol., 77, 848-854.
4. Bayram, E., Karaman, C., Kuru, Z. and Karaman, O. 2021, Water Supply, 21, 157-165.
5. Yuan, S., Lai, Q., Duan, X. and Wang, Q. 2023, J. Energy Storage, 61, 106716.
6. Su, L., Jing, Y. and Zhou, Z. 2011, Nanoscale, 3, 3967.
7. Aravindan, V., Lee, Y. and Madhavi, S. 2015, Adv. Energy Mater., 5.
8. Bhatt, M. D. and Lee, J. Y. 2019, Int. J. Hydrogen Energy, 44, 10852-10905.
9. Sonia, F. J., Aslam, M. and Mukhopadhyay, A. 2020, Carbon N. Y., 156, 130-165.
10. Mukhopadhyay, A. and Sheldon, B. W. 2014, Mater. Sci., 63, 58-116.
11. Sui, D., Si, L., Li, C., Yang, Y., Zhang, Y. and Yan, W. 2021, Chemistry (Easton)., 3, 1215-1246.
12. Liu, Z., Tian, Y., Wang, P. and Zhang, G. 2022, Front. Nanotechnol., 4.
13. Bayram, E., Yilmaz, G. and Mukerjee, S. 2016, Appl. Catal. B Environ., 192, 26-34.
14. Li, G., Huang, B., Pan, Z., Su, X., Shao, Z. and An, L. 2019, Energy Environ. Sci., 12, 2030-2053.

15. Bayram, E. and Sungur, B. 2023, ChemElectroChem, 10.
16. Yabuuchi, N., Kubota, K., Dahbi, M. and Komaba, S. 2014, Chem. Rev., 114, 11636-11682.
17. Bayram, E. and Ayranci, E. 2012, J. Electroanal. Chem., 683, 14-20.
18. Zhang, Y., Xia, X., Liu, B., Deng, S., Xie, D., Liu, Q., Wang, Y., Wu, J., Wang, X. and Tu, J. 2019, Adv. Energy Mater., 9.
19. Irisarri, E., Ponrouch, A. and Palacin, M. R. 2015, J. Electrochem. Soc., 162, A2476-A2482.
20. Ma, G., Huang, K., Zhuang, Q. and Ju, Z. 2016, Mater. Lett., 174, 221-225.
21. Sungur, B., Kızıl, Ç. and Bayram, E. 2023, Int. J. Hydrogen Energy, 48, 17512-17525.
22. Cui, H., Zheng, J., Yang, P., Zhu, Y., Wang, Z. and Zhu, Z. 2015, ACS Appl. Mater. Interfaces, 7, 11230-11238.
23. Fu, X., Jin, J., Liu, Y., Wei, Z., Pan, F. and Zhang, J. 2014, ACS Appl. Mater. Interfaces, 6, 3930-3936.
24. Çakmak, G. and Öztürk, T. 2019, Diam. Relat. Mater., 96, 134-139.
25. Xiao, B., Rojo, T. and Li, X. 2019, ChemSusChem, 12, 133-144.
26. Raccichini, R., Varzi, A., Chakravadhanula, V. S. K., Kübel, C. and Passerini, S. 2016, Sci. Rep., 6, 23585.